Fabry-Pérot and Friedrich-Wintgen bound states in the continuum in a photonic triple-stub cavity

Yamina Rezzouk [1], Soufyane Khattou [1], Mohamed El Ghafiani [1], Madiha Amrani [1], El Houssaine El Boudouti [1,*]
Abdelkrim Talbi [2], and Bahram Djafari-Rouhani [3]

[1]*LPMR, Département de Physique, Faculté des Sciences, Université Mohammed I, 60000 Oujda, Morocco*
[2]*University of Lille, CNRS, Centrale Lille, University Polytechnique Hauts-de-France, UMR 8520-IEMN, F-59000 Lille, France*
[3]*IEMN, UMR CNRS 8520, Département de Physique, Université de Lille, 59655 Villeneuve d'Ascq, France*

Bound states in the continuum (BICs) are zero-width (infinite lifetime) trapped eigenmodes that remain confined in the system even though they coexist with a continuum of extended states. The resulting high-frequency resonances may have significant applications in photonic integrated circuits, filtering, sensing, and laser. In this paper, we demonstrate that a simple design based on a photonic triple-stub cavity can display both Fabry-Pérot (FP) and Friedrich-Wintgen (FW) BICs, and their occurrence is very dependent on the way the cavity is attached to the outside medium by one or two ports. We first consider a symmetric cavity where a stub of length d_3 is surrounded by two stubs of length d_2, and all stubs are separated by segments of length d_1. When the cavity is inserted between two ports, we demonstrate theoretically and validate experimentally the existence of symmetric BICs (S-BIC) and antisymmetric BICs (AS-BIC) of FP type under commensurability conditions between the lengths d_1, d_2, and d_3. The S-BICs and AS-BICs may cross each other, giving rise to a doubly degenerate BIC. By breaking the symmetry of the cavity, AS-BICs and S-BICs can couple together and realize a FW-type BIC where one resonance remains with zero width while the other broadens into a bright mode. By considering two additional configurations where the triple-stub cavity is attached with one or two ports from only one side, additional BICs can be induced inside the structure. By slightly detuning from the BIC condition, the latter transforms into either an electromagnetic-induced transparency/reflection or Fano resonance. Finally, such a triple-stub cavity can be designed to realize near-perfect absorption for some frequencies. All the analytical results, obtained from the Green's function method, have been confirmed experimentally in the radiofrequency domain using coaxial cables.

I. INTRODUCTION

The interaction of electromagnetic waves with scatterers in a composite material generates resonances and antiresonances in the transmission spectra [1]. In photonic circuits, these important phenomena have been shown both theoretically and experimentally, including Fano [2,3], electromagnetic-induced transparency (EIT) [4,5], and electromagnetic-induced reflection (EIR) resonances [6]. In Fano resonance [7], the peak is followed by antiresonance in a narrow frequency range, giving rise to an asymmetrical line profile shape. When the resonance falls between two antiresonances (resonances), Fano resonance acts like EIT (EIR) resonance [8]. These resonances (antiresonances) are the result of a discrete localized mode interacting with a continuum of propagating modes, which can transform an opaque (transparent) system into a transparent (opaque) one in a narrow frequency range. In addition to Fano, EIT, and EIR resonances, bound states in the continuum (BICs) [9] have found a high amount of interest in recent years [10–12]. These nonradiating modes are localized within a continuum of extended modes, yet they remain highly confined with an infinite lifetime and quality factor (Q factor) in lossless systems. Hence, BICs remain well confined in some parts of the system, even though they coexist with a continuous spectrum of outgoing waves that can transport energy away. BIC, Fano, and EIT phenomena were observed in quantum systems [7–9]; however, it was shown that these resonances can be extended to different classical systems such as photonic systems [13–18], plasmonic nanostructures [12,19–21], metasurfaces [22–24], and fiber Bragg gratings [25].

The physical mechanisms behind the formation of BICs may be split into three main categories [10]: BICs protected by symmetry or separability (SP) BICs [26], Friedrich-Wintgen (FW) BICs [27] and Fabry-Pérot (FP) BICs [28], which have been extensively investigated [21,24,29–37]. SP-BICs refer to the incompatibility of symmetry between two sets of modes, i.e., a bound state with one symmetry class may fall into a continuum state with another class of symmetry without any coupling between them [26,29]. FP-BICs refer to destructive interference when two resonant cavities are spaced apart so that they are tuned to make the roundtrip phase shift add up to an integer multiple of 2π, causing destructive interference between the two resonances and then

---
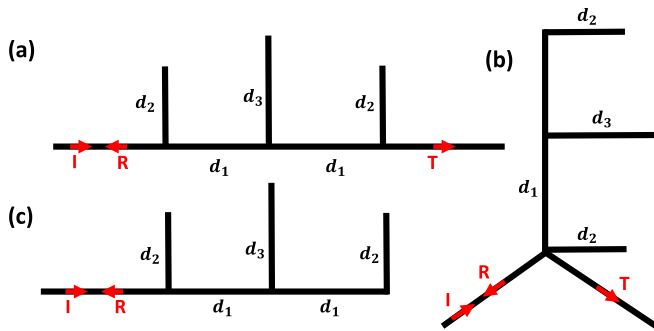
*Contact author: elboudouti@yahoo.fr

FIG. 1. (a) Schematic of a symmetric triple-stub cavity composed of a stub of length d_3 inserted between two stubs of length d_2 and separated by a segment of length d_1. (b) The symmetric cavity is attached vertically to two ports from one side. (c) The symmetric cavity is attached only to one port from one side. I, R, and T denote the incident, reflected, and transmitted waves, respectively.

the formation of a BIC [31,32]. The resonances leading to FW-BICs belong to the same cavity and are coupled through the same radiation channel. Further, this BIC results from the interaction of two resonant modes with an avoided crossing, and at a specific parameter value, the width of one resonance vanishes, resulting in a FW-BIC, while the other resonance becomes more lossy [18,24]. In addition to the abovementioned BICs existing in simple cavities, there are other types of BICs in periodic structures including BICs at the Γ and off-Γ points of band structures [26,38,39] as well as BICs due to either Brillouin zone folding [40] or momentum mismatch in compound grating waveguide structures [41]. The realization of BICs in photonics was discussed [28], followed by an experimental demonstration of optical BICs [42]. Since then, there has been increasing interest due to their infinitely high-Q factor in lossless systems [38,43,44], with practical applications such as ultrasensitive optical absorption [45,46], strong light enhancement [12], and photonic integrated circuits [47]. Additionally, BICs give rise to discontinuities in the transmission and reflection coefficients, which can offer a wide range of applications, including sensors [21,48–50], lasers [51–53], and filters [54].

In a recent paper [18], we have studied FW-BIC and EIT resonances within a simple T-shaped cavity coupled laterally to a waveguide. We have also used photonic stubbed structures featuring double stubs [1,13] to investigate FP-BIC, EIT, and Fano resonances. This cavity with two resonators (stubs) is a FP kind cavity that presents symmetric and antisymmetric modes. Notably, when the roundtrip phase shift adds up to 2π, one of the two resonances becomes a BIC. However, within this configuration, symmetric and antisymmetric modes operate independently without any interaction with each other. Here, we propose a symmetric triple-stub cavity made up of a stub of length d_3 surrounded by two stubs of length d_2 and separated by segments of length d_1 (see Fig. 1). The whole cavity is inserted between two ports. The main advantages of this structure are the existence of both symmetric and antisymmetric resonant modes that can cross each other. The antisymmetric modes are independent of stub d_3, as the latter is located in the middle of the cavity where the electric field vanishes, whereas the symmetric modes depend on the

geometrical parameters of the whole system. We show that, when d_1, d_2, and d_3 are chosen appropriately commensurate, the antisymmetric BIC (AS-BIC) is independent of d_3. However, the symmetric BIC (S-BIC) appears when the width of the S resonance vanishes. The crossing between the S-BIC and AS-BIC gives rise to a doubly degenerate BIC (D-BIC). The AS-BIC and S-BIC in the symmetric cavity [Fig. 1(a)] can be qualified as FP-BICs. When the symmetry of the cavity is broken by slightly detuning one of the two stubs of length d_2 by a small amount δ, we obtain an avoided crossing of the two modes leading to a FW-BIC. Therefore, compared with the double-stub cavity, the triple-stub cavity may exhibit a crossing and avoided crossing between symmetric and antisymmetric modes, leading to the formation of either a FP-BIC or a FW-BIC. Also, we provide an analysis of the mechanism behind the FW-BIC and FP-BIC and the possibility of switching from one to another in the triple-stub cavity. The number of BICs in a cavity depends on the number of channels surrounding it. Indeed, BICs are an outcome of destructive interference through parameter tuning across various channels. Tuning a significant number of system parameters can lead to the complete elimination of radiation and, as a result, the generation of a BIC. In general, if radiation contains N degrees of freedom, at least N parameters need to be adjusted to obtain a BIC [10,55]. Such suppression can be interpreted as an interference effect in which two or more radiating components cancel each other out. Here, we show that, apart from the BICs in the symmetric cavity inserted between two ports from two sides [Fig. 1(a)], other BICs can occur when the cavity is attached to either two ports [Fig. 1(b)] or just one port [Fig. 1(c)] from only one side. Furthermore, by deviating from the BIC condition, the latter transforms into EIT, EIR, or Fano resonance. In addition, the triple-stub cavity can be used to achieve near-perfect absorption at some frequencies. The analytical results are obtained from an analysis of the transmission and reflection coefficients as well as the density of states (DOS) using the Green's function method [1]. The DOS is defined as the number of states by units of angular frequency [56]. Also, we provide a comparison between DOS and the derivative of the argument of the determinant of the scattering matrix (the so-called Friedel phase [57–59]) as well as the reflection delay time. The analytical results are confirmed by experiments carried out using coaxial cables in the radiofrequency regime. Let us mention also that all the results presented here for photonic circuits can be transposed to metal-insulator-metal (MIM) plasmonic nanowaveguides operating in the infrared domain [18,21]. We present a numerical example in the Supplemental Material [60] and focus here on the theoretical demonstrations that can be compared with our experimental measurements.

This paper is structured as follows: In Sec. II, we present an analytical and experimental comparative study of the transmission spectra and the DOS through a symmetric and asymmetric triple-stub cavity inserted between two ports [Fig. 1(a)]. In Sec. III, we discuss both theoretically and experimentally the transmission and reflection spectra for the cavity attached to two or one port from one side [Figs. 1(b) and 1(c)], leaving the other side free. The conclusion is given in Sec. IV.

II. TRIPLE-STUB CAVITY WITH TWO PORTS FROM TWO SIDES

A. Symmetric cavity-induced FP-BIC

The cavity under study consists of a symmetric triple-stub cavity composed of a stub of length d_3 inserted between two stubs of length d_2 and separated by a segment of length d_1. The whole cavity is inserted between two semi-infinite waveguides [Fig. 1(a)]. Moreover, the boundary condition at the ends of the stubs is a vanishing magnetic field ($H = 0$). For our

study, the lengths d_1 and d_2 are chosen to be fixed, while d_3 is taken variable. The calculation approach, which is based on the Green's function method [1], enables us to deduce different properties of the cavity, including the transmission and reflection coefficients as well as the eigenmodes of the isolated cavity. The expression of the transmission and reflection coefficients through the symmetric cavity [Fig. 1(a)] is given as follows (for more details, see Supplemental Material SM1 [60]):

$$t_h = \frac{2C_2^2 C_3}{\{(C_1 C_2 - S_1 S_2) - jS_1 C_2\}\{C_2(2C_1 C_3 - S_1 S_3) - j[2C_3(C_1 S_2 + S_1 C_2) + S_3(C_1 C_2 - S_1 S_2)]\}}, \tag{1a}$$

and

$$r_h = \frac{C_1 C_2^2 (2S_1 C_3 + C_1 S_3) + (2C_1 C_3 - S_1 S_3)(2C_1 C_2 S_2 - S_1) - 2C_2 C_3 S_2}{\{(C_1 C_2 - S_1 S_2) - jS_1 C_2\}\{C_2(2C_1 C_3 - S_1 S_3) - j[2C_3(C_1 S_2 + S_1 C_2) + S_3(C_1 C_2 - S_1 S_2)]\}}, \tag{1b}$$

where $C_i = \cos(kd_i)$, $S_i = \sin(kd_i)$, and $k = \frac{\omega\sqrt{\varepsilon}}{c}$. Here, ω is the angular frequency, ε is the dielectric permittivity of the waveguide, and c is the speed of light in vacuum. For a lossless system, one can deduce from Eqs. (1a) and (1b) that the transmission and reflection rates verify the conservation energy law $|t_h|^2 + |r_h|^2 = 1$.

It is well known that the eigenmodes of the whole system [Fig. 1(a)] can be obtained from the poles of the Green's function or equivalently from the denominator of the transmission/reflection coefficients [Eqs. (1a) and (1b)], namely,

$$\{(C_1 C_2 - S_1 S_2) - jS_1 C_2\}\{C_2(2C_1 C_3 - S_1 S_3)$$
$$- j[2C_3(C_1 S_2 + S_1 C_2) + S_3(C_1 C_2 - S_1 S_2)]\} = 0. \tag{2}$$

As predicted, Eq. (2) gives two decoupled solutions corresponding to symmetric and antisymmetric modes of the system, namely,

$$C_1 C_2 - S_1 S_2 - jS_1 C_2 = 0 \tag{3a}$$

and

$$C_2(2C_1 C_3 - S_1 S_3)$$
$$- j[2C_3(C_1 S_2 + S_1 C_2) + S_3(C_1 C_2 - S_1 S_2)] = 0, \tag{3b}$$

respectively.

One can clearly see that the antisymmetric modes given by Eq. (3a) are independent of stub d_3, whereas the symmetric modes provided by Eq. (3b) depend on the geometrical parameters of the whole system. As previously mentioned, the poles of t_h and r_h [Eq. (2)] refer to bound states. Indeed, Eqs. (3a) and (3b) are complex quantities; their imaginary parts are responsible for the broadening of resonances in the transmission coefficient, while their real parts give the position of the resonance. However, when the real and imaginary parts of Eqs. (3a) and (3b) vanish together at the same frequency, then we get trapped modes (BICs) in the continuum. These BICs appear as resonances with zero width in the transmission and reflection spectra as well as in the DOS. The solution of Eq. (3a) leads to the following simple equation, giving rise to

antisymmetric BICs (AS-BIC):

$$S_1 = 0 \quad \text{and} \quad C_2 = 0. \tag{4}$$

From Eq. (4), one can deduce

$$kd_1 = n_1 \pi \quad \text{and} \quad kd_2 = (2m_2 + 1)\frac{\pi}{2}, \tag{5a}$$

and therefore, the commensurability between d_1 and d_2, such that

$$\frac{d_2}{d_1} = \frac{2m_2 + 1}{2n_1}, \tag{5b}$$

where m_2 is an integer and n_1 is a nonzero integer. As mentioned above, the AS-BIC is independent of d_3, as the corresponding electric field presents a node in the middle of the triple-stub cavity where stub d_3 is inserted, while an analysis of Eq. (3b) leads to two types of solutions associated with S-BICs, namely,

$$S_1 = 0, \quad C_2 = 0, \quad \text{and} \quad C_3 = 0, \tag{6a}$$

and

$$C_1 = 0, \quad C_2 = 0, \quad \text{and} \quad S_3 = 0. \tag{6b}$$

One can see that Eq. (6a) gives a solution that leads to both the S-BIC and AS-BIC [Eq. (4)]; hence, we get a D-BIC. Indeed, Eq. (6a) is fulfilled when d_1, d_2, and d_3 satisfy both Eq. (5b) and the following equation about the commensurability of d_3 and d_1:

$$\frac{d_3}{d_1} = \frac{2m_3 + 1}{2n_1}. \tag{7}$$

Therefore, Eqs. (5b) and (7) give the conditions that should be satisfied by d_1, d_2, and d_3 to get a D-BIC. As mentioned above, the BICs are given by the poles of the transmission coefficient; however, at these frequencies, the transmission does not diverge, as the numerator of the transmission vanishes also, giving rise to a finite value in the transmission amplitude. For example, let us take $n_1 = 1$, $m_2 = m_3 = 0$ (i.e., $d_2 = d_3 = \frac{d_1}{2}$). In this case, we can easily show that the expression of the

transmission [Eq. (1a)] becomes simply

$$t_h = \frac{2C_2}{2C_2 - 3jS_2}.$$ (8)

From Eq. (8), one can deduce the transmission rate as

$$T = |t_h|^2 = \frac{4C_2^2}{5S_2^2 + 4}.$$ (9)

The latter equation clearly shows that the transmission rate is finite at the BIC frequency given by $C_2 = 0$; T vanishes here.

The second solution which yields the S-BIC [Eq. (6b)] gives

$$kd_1 = (2m_1 + 1)\frac{\pi}{2}, \quad kd_2 = (2m_2 + 1)\frac{\pi}{2},$$

$$kd_3 = n_3\pi.$$ (10a)

Therefore, d_1, d_2, and d_3 should be chosen commensurate, such that

$$\frac{d_2}{d_1} = \frac{(2m_2 + 1)}{(2m_1 + 1)}$$ (10b)

and

$$\frac{d_3}{d_1} = \frac{2n_3}{(2m_1 + 1)},$$ (10c)

where m_1 is an integer and n_3 is a nonzero integer.

Another interesting physical quantity that can be obtained from the Green's function is the DOS. This quantity is related to the determinant of the scattering matrix S' defined by

$$S' = \begin{pmatrix} r_h & t_h \\ t_h & r_h \end{pmatrix},$$ (11)

where t_h and r_h are given by Eqs. (1a) and (1b), respectively.

Indeed, for a lossless system, the determinant of the scattering matrix S' can be obtained from the expressions of t_h and r_h as $\det(S') = r_h^2 - t_h^2$ since the cavity is symmetric. The scattering Friedel phase θ_F for the lossless system is given by [57–59],

$$\theta_F = \arg[\det(S')].$$ (12)

Moreover, it was shown [58,59] that the variation of DOS [$\Delta n(\omega)$] between the final and initial systems is related to the Friedel phase θ_F by the following expression (see Supplemental Material SM2 [60]):

$$\frac{d\theta_F}{d\omega} = 2\pi \Delta n(\omega).$$ (13)

In our case, the final and initial systems consist of the triple-stub cavity coupled to or decoupled from the two semi-infinite wires. In a lossless system, the derivative of the Friedel phase $\frac{d\theta_F}{d\omega}$ behaves similarly compared with the DOS. These findings show that the DOS can be extracted from the measurement of the argument of the determinant of the scattering matrix [Eq. (13)]. However, for a lossy system, Eq. (13) is no longer valid, and $\frac{d\theta_F}{d\omega}$ can exhibit a different behavior in comparison with the DOS [61].

Before going into the details of the BICs induced by the stub of length d_3 for given d_1 and d_2 [Fig. 1(a)], let us first give a comparison of the BICs for two particular cavities, namely, $d_3 = 0$ [Fig. 2(a)] and $d_3 = d_2$ [Fig. 2(c)]. In the first case (i.e.,
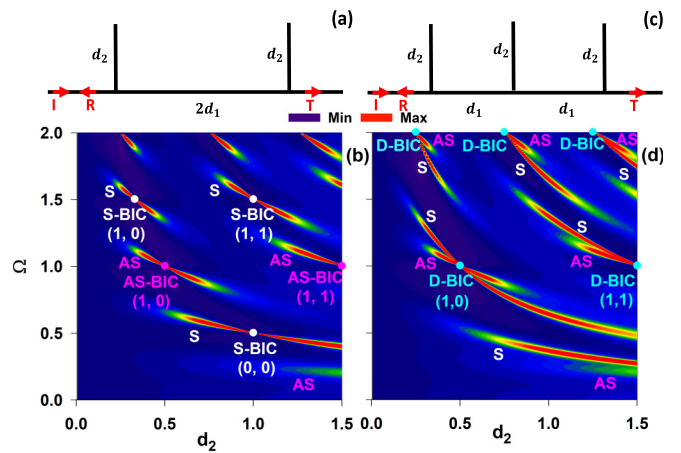

FIG. 2. (a) Fabry-Pérot (FP) cavity made up of double stubs of length d_2 and separated by a segment of length $2d_1$. (c) Triple-stub cavity made of segments of length d_1 and stubs of length d_2. (b) and (d) Variation of the density of states (DOS) in color scale as a function of Ω and stub d_2 for lossless cavities in (a) and (c), respectively. The full white, pink, and cyan circles indicate the position of the symmetric, antisymmetric, and doubly degenerate bound states in the continuum (S-BICs), (AS-BICs), and (D-BICs), respectively.

$d_3 = 0$), the S-BIC and AS-BIC are given by the geometrical parameters [Eqs. (5b) and (10b)] and the corresponding frequencies [Eqs. (5a) and (10a)], respectively. Here, the S-BIC and AS-BIC cannot hold simultaneously.

An example of the dispersion curves from the DOS is given in color scale as a function of Ω and stub d_2 in Fig. 2(b). All lengths are given in units of $d_1 = 1$ m, and the dimensionless frequency $\Omega = \frac{kd_1}{\pi}$ is used. Different S-BICs (white circles) and AS-BICs (pink circles) associated with the pairs (m_1, m_2) and (n_1, m_2) in Eqs. (10b) and (5b) are reported. In the second case (i.e., $d_3 = d_2$), the S-BIC and AS-BIC are given by Eqs. (4) and (6a). Here, both BICs fall at the same frequency [Eq. (5a)], giving rise to a D-BIC. The dispersion curves obtained from the DOS are shown in Fig. 2(d); we can see the dispersion of the symmetric and antisymmetric resonances giving rise to a D-BIC at the crossing points. The BICs corresponding to different pairs (n_1, m_2) in Eq. (5b) are represented by cyan circles in Fig. 2(d). Consequently, one of the advantages of introducing stub d_3 results in the crossing between the S-BIC and AS-BIC, giving rise to a D-BIC. This property enables us to study the interaction between the two FP-BICs by varying the length of stub d_3.

In the following, we will give a numerical and experimental validation of the analytical results about the existence of FP-BICs in the triple-stub cavity [Fig. 1(a)] with d_1 and d_2 fixed, while d_3 is variable. We will discuss in detail two cases: (i) the case where both AS-BIC and S-BIC hold simultaneously [Eqs. (4) and (6a)] and (ii) the case where only the S-BIC occurs [Eq. (6b)]. For the first case, we chose $\frac{d_2}{d_1} = \frac{1}{2}$ [i.e., $m_2 = 0$ and $n_1 = 1$ in Eq. (5b)] and d_3 variable. This choice of geometrical parameters enables us to get both AS-BIC and S-BIC at $\Omega = \frac{kd_1}{\pi} = 1$ [Eq. (5a)]. Figure 3(a) shows the transmission intensity (in color scale) vs Ω and d_3 through the lossless FP cavity [Fig. 1(a)]. The horizontal white dotted line at $\Omega = 1$ indicates the position of the AS-BIC, which is independent
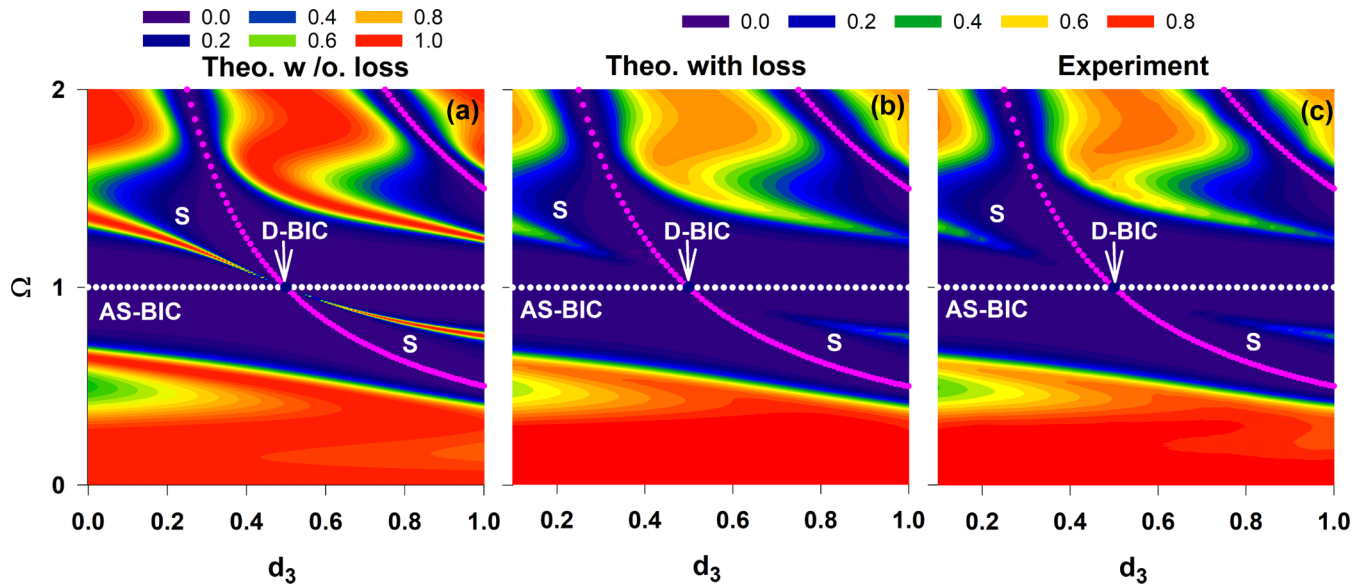
FIG. 3. Theoretical variation of the transmission magnitude (in color scale) vs Ω and d_3 in the (a) lossless and (b) lossy systems. (c) Experimental validation of the transmission magnitude through the lossy cavity [Fig. 1(a)]. The white and pink dotted points represent the transmission zeros induced by stubs d_2 and d_3, while the white arrow indicates the position of the doubly degenerate bound state in the continuum (D-BIC).

of d_3 and coincides with the transmission zero induced by stub d_2. Around $\Omega = 1$, there exists a resonance labeled S with nonzero width, which depends on d_3. This resonance corresponds to the symmetric mode given by Eq. (3b). One can observe a shrinking of the S resonance as d_3 increases, which appears as a transparency window between two zeros (denoted by pink and white dotted points). As predicted, this resonance disappears for $d_3 = \frac{1}{2}$ [i.e., $m_3 = 0$ and $n_1 = 1$ in Eq. (7)], giving rise to the S-BIC. The crossing of the AS-BIC and S-BIC for $d_3 = \frac{1}{2}$ and $\Omega = 1$ gives rise to a D-BIC. For $d_3 > 0.5$, the S resonance reappears when we shift slightly from the BIC position. Figure 3(b) shows the same results as in Fig. 3(a), when loss in the cables is considered. However, due to the loss, the intensity of the S resonance around $\Omega = 1$ becomes weak when the width of the latter tends to zero. For comparison, the findings of the experimental analysis are presented in Fig. 3(c), where we can see good agreement between theory and experiment. It is worth mentioning that the measurements were carried out in the radiofrequency domain using standard coaxial cables (RG-58/U) of various lengths with the same characteristic permittivities and impedances ($Z = 50$). Polyethylene was used to fill the cables ($\varepsilon' = 2.3$), which corresponds to a typical propagation speed of $0.66c$. The attenuation inside the coaxial cables was simulated by introducing a complex dielectric permittivity $\varepsilon = \varepsilon' - j\varepsilon''$. The attenuation coefficient can be expressed as $\alpha'' = \frac{\varepsilon'' \omega}{c \sqrt{\varepsilon'}}$. The experimental setup and more details about the experimental procedure are given in Supplemental Material SM3 [60].

To gain a better understanding of the behavior of the resonant modes as well as the BICs close to $d_3 = \frac{1}{2}$ and $\Omega = 1$, we plotted in Figs. 4(a)–4(e) some transmission spectra as a function of Ω for given values of d_3. The blue curves represent the transmission for a lossless system, while the green dashed curves are plotted by considering losses. Experimental

measurements, shown by red open circles, validate the theoretical results. The vertical arrows at $\Omega = 1$ indicate the position of the AS-BIC in the transmission spectra; it appears as a resonance with zero width, whatever the value of d_3. Moreover, the two transmission zeros induced by stubs d_2 and d_3 (white and pink branches in Fig. 3) are indicated by black circles on the frequency axis. The S resonance lying between these two transmission zeros behaves as EIT resonance. To confirm that the resonance is of EIT type, we have fitted the results of the transmission coefficients by the EIT formula [4] (see Supplemental Material SM4 [60]). For $d_3 < \frac{1}{2}$ [Figs. 4(a) and 4(b)], the S resonance falls above $\Omega = 1$; its width decreases as d_3 increases, giving rise to the S-BIC for $d_3 = \frac{1}{2}$ [Fig. 4(c)]. The mergence of the S-BIC and AS-BIC at $d_3 = \frac{1}{2}$ leads to a D-BIC. For $d_3 > \frac{1}{2}$, the S-BIC transforms again to an S resonance below $\Omega = 1$; its width increases as far as d_3 is far from $\frac{1}{2}$ [Figs. 4(d) and 4(e)].

COMSOL Multiphysics software based on the finite element method can also be used to conduct numerical simulations to obtain similar results as in the analytical approach, including the transmission and reflection coefficients. This numerical method enables us to solve the transmission line equations, telegrapher's equations, and electromagnetic wave equations efficiently (for further details, see chap. 16 in Ref. [1]). Let us point out that we used a mesh grid comprising 2500 elements distribution for the simulations. We conducted convergence tests to ensure the accuracy and reliability of our results. Moreover, the running time for the simulations was very rapid, taking less than a minute to complete. An example comparing COMSOL results with analytical and experimental results is provided in Supplemental Material SM5 [60]. One of the benefits of using COMSOL lies in its facilities to obtain electric field distribution inside the different waveguides, which is easier than using the Green's function method. An example of
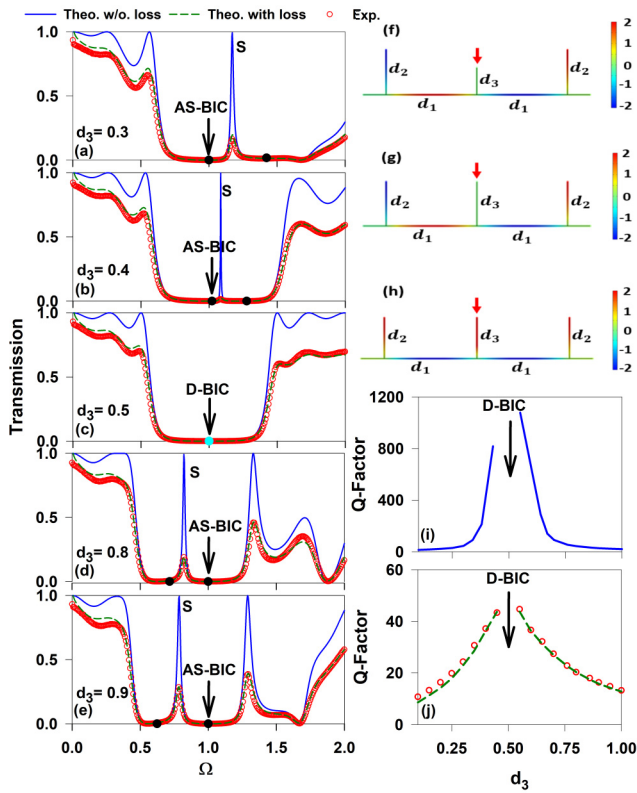
FIG. 4. (a)–(e) Transmission spectra for various lengths of stub d_3 through the cavity [Fig. 1(a)]. The full black circles indicate the position of the transmission zeros, while the black arrows indicate the bound state in the continuum (BIC) positions. (f)–(h) Electric field map at $\Omega = 1$ of the antisymmetric BIC (AS-BIC) for (f) $d_3 = 0.3$ and (g) $d_3 = 0.5$ and (h) the symmetric BIC (S-BIC) for $d_3 = 0.5$. The red arrows in (f)–(h) indicate the excitation position. (i) and (j) Quality factor of the S resonance as a function of stub d_3. Blue and green curves represent theoretical results in the absence and presence of loss, respectively, while the red open circles represent experimental validation.

the electric field distribution associated with the AS-BIC and S-BIC within the triple-stub cavity is illustrated in Figs. 4(f)–4(h). By applying a local electric excitation source at the border of stub d_3, we plot the electric field map of the AS-BIC for $d_3 = 0.3$ [Fig. 4(f)] and the D-BIC for $d_3 = d_2 = 0.5$ [Figs. 4(g) and 4(h)] at $\Omega = 1$, respectively. The BICs are tightly confined inside the cavity without emitting any external radiation. These modes are stationary waves; the electric field vanishes at the junction points, with either antisymmetric [Figs. 4(f) and 4(g)] or symmetric [Fig. 4(h)] behavior. Also, the electric field reaches its maximum at the end of the stubs as the boundary conditions at these points are $H = 0$. However, as predicted, for the AS-BIC [Figs. 4(f) and 4(g)], the electric field in stub d_3 vanishes, as this mode is independent of d_3. As mentioned before, the BIC is characterized by a high-Q factor (infinite lifetime). In Fig. 4(i), we presented the Q factor of the S resonance in the absence of loss (blue curve), whereas Fig. 4(j) shows the same results in the presence of loss theoretically (green curve) and experimentally (red circles). As shown in Figs. 4(a)–4(e), we can control the Q factor of the

S resonances by varying d_3. As d_3 increases, we observe a continuous increase in the Q factor of the resonance due to the shrinking of its width. At the critical value of $d_3 = \frac{1}{2}$, the two transmission zeros overlap, and as a result, the Q factor of the resonance squeezed between them becomes infinite. It is noted that, even in the presence of losses [Fig. 4(j)], the Q factor is still defined but with lower values than in the lossless system and reaches a higher value when d_3 tends toward 0.5.

The variation of the DOS [$\Delta n(\omega)$], as earlier indicated [Eq. (13)], can be extracted from the argument of the determinant of the scattering matrix. Figure 5(a) shows the variation of the DOS (in color scale) as a function of Ω and d_3. At $\Omega = 1$, there exists an AS-BIC indicated by the horizontal dashed lines. The frequency of the symmetric resonant mode S decreases as a function of d_3; its width tends to zero for $d_3 = \frac{1}{2}$, giving rise to a S-BIC, as illustrated in Fig. 5(b). The crossing of the S-BIC and AS-BIC at $\Omega = 1$ and $d_3 = \frac{1}{2}$ gives rise to the D-BIC. Some examples of the DOS spectra (blue curves) and the derivative of the Friedel phase $\frac{d\theta_F}{d\omega}$ (green dashed curves) are given in Figs. 5(c)–5(g) for various lengths of d_3. As d_3 increases [Figs. 5(c) and 5(d)], one can see, in addition to the AS-BIC indicated by the vertical arrow, the transformation of the S resonance into a hidden resonance at $d_3 = \frac{1}{2}$ as a signature of the S-BIC [Fig. 5(e)]. The BIC appears as a delta peak in the DOS with an infinite lifetime (zero-width resonance), whereas when we shift from the S-BIC position, this latter transforms into a classical Breit-Wigner resonance, characterized by a finite width related to its lifetime. Moreover, when d_3 increases [Figs. 5(f) and 5(g)], the frequencies of the corresponding modes decrease below $\Omega = 1$. As previously stated, for a lossy system, the analytical finding [Eq. (13)] is no longer applicable when det(S') tends to zero, and as a result, $\frac{d\theta_F}{d\omega}$ behaves differently from the DOS. Indeed, the derivative of the Friedel phase exhibits a negative peak at the resonance, as illustrated in Figs. 5(c), 5(d), 5(f), and 5(g). This can be explained by the fact that det(S') vanishes at this position (i.e., $t = \pm r$) and changes sign, leading to an abrupt phase change of π in the phase of det(S') and hence a negative peak in $\frac{d\theta_F}{d\omega}$. The experimental results of $\frac{d\theta_F}{d\omega}$ (red open circles) and the theoretical ones in the presence of loss (green dashed lines) show good agreement.

In what follows, we will discuss the second solution, which leads to the S-BIC [Eq. (6b)]. For this reason, we have chosen $d_2 = \frac{1}{3}$ [i.e., $m_2 = 0$ and $m_1 = 1$ in Eq. (10b)] and d_3 variable. In this case, the S-BIC is expected for $d_3 = \frac{2}{3}$ [i.e., $n_3 = 1$, $m_1 = 1$ in Eq. (10c)] and $\Omega = \frac{3}{2}$ [Eq. (10a)]. Here, the S-BIC does not cross any AS-BIC, as Eq. (5b) is not satisfied. Hence, to give better insight into the evolution of the symmetric resonant modes as well as their conversion to the S-BIC, we have plotted in Fig. 6(a) the transmission magnitude through the symmetric cavity [Fig. 1(a)] for $d_2 = \frac{1}{3}$. The horizontal white dotted line at $\Omega = \frac{3}{2}$ gives the position of the transmission zeros induced by stub d_2 (i.e., $C_2 = 0$). As predicted, we can see the appearance of the S resonance around $\Omega = \frac{3}{2}$ and its transformation to a BIC at $d_3 = \frac{2}{3}$. Around $d_3 = \frac{2}{3}$, the S resonance falls near transmission zero, so the latter can behave as Fano resonance (see below). The behavior of the electric field associated with the S-BIC is given in Fig. 6(b) for $d_3 = \frac{2}{3}$ at $\Omega = \frac{3}{2}$. As predicted, the S-BIC is localized in
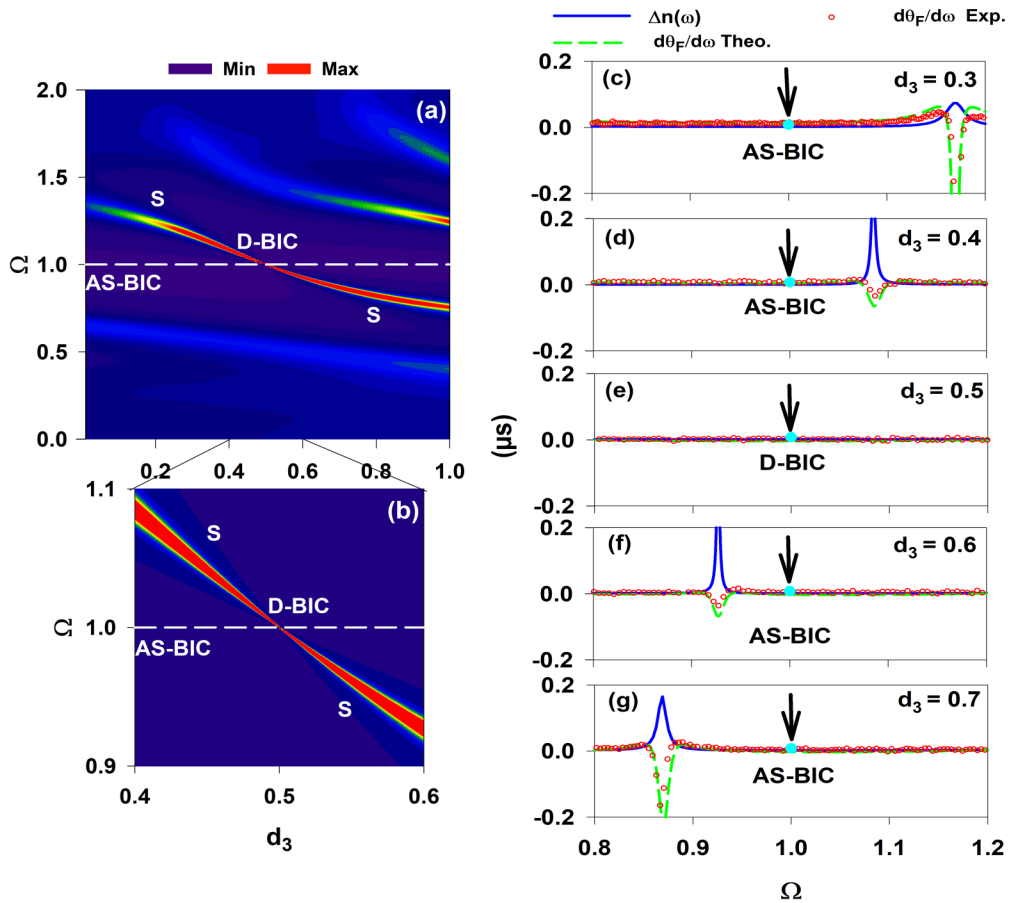
FIG. 5. (a) Variation of the density of states (DOS) in color scale as a function of Ω and stub d_3 in the lossless system. (b) Zoom of the DOS around $d_3 = 0.5$ and $\Omega = 1$. (c)–(g) DOS spectra (blue lines) and the derivative of the Friedel phase $\frac{d\theta_F}{d\omega}$ for some values of d_3. The theoretical results of $\frac{d\theta_F}{d\omega}$ (green dashed lines) are validated by the experimental measurements (red open circles) for the lossy system. The vertical arrows indicate the position of the antisymmetric bound state in the continuum (AS-BIC).

the cavity with a symmetric shape and does not extend beyond it. Moreover, each stub exhibits the maximum electric field at its termination. In Figs. 6(c)–6(g), we have theoretically sketched some transmission spectra without (blue curves) and with (green dashed curves) losses. The experimental results (red circles) are in good agreement with the theoretical results in the presence of loss. The black circle at $\Omega = \frac{3}{2}$ corresponds to the transmission zero induced by stub d_2. It is worth mentioning that the S resonance appears as Fano resonance. To ensure that the transmission resonance exhibits a Fano-like shape, we have performed the Fano formula [2], as shown in Supplemental Material SM4 [60]. Moreover, one can see the transformation of the S resonance into the S-BIC, which appears as a hidden resonance for $d_3 = \frac{2}{3}$ and $\Omega = \frac{3}{2}$ [marked by a vertical arrow in Fig. 6(e)], whereas by slightly varying the length d_3 from the BIC position, the S-BIC opens up and becomes a Fano resonance characterized by a finite width.

B. Asymmetric cavity-induced FW-BIC

To introduce a coupling between the AS-BIC and S resonance in Figs. 3(a) and 5(a), we break the symmetry of the triple-stub cavity in Fig. 1(a) by changing slightly the stub of length d_2 on the right side by a stub of length $d_2' = d_2 - \delta$.

Therefore, the cavity becomes asymmetric, and it is no longer of FP type. Figures 7(a) and 7(b) show the variation of the intensity of the DOS and transmission (in color scale) as a function of Ω and d_3 for $\delta = 0.2$. Figure 7(a), displaying the DOS, clearly shows the transformation of the AS-BIC at $\Omega = 1$ in Fig. 5(a) to a resonance of finite width above $\Omega = 1$. Furthermore, we observe an anticrossing between the two resonances at $d_3 = 0.5$. There is a lifting of the degeneracy of the D-BIC in Fig. 7(a) where only one BIC remains at $\Omega = 1$ and $d_3 = 0.5$, while the second BIC transforms to a resonance with finite width. Indeed, one can see the shrinking of the lower resonance width giving rise to a BIC at $d_3 = 0.5$ (denoted by the white arrow), whereas the width of the upper resonance remains almost constant and less affected by stub d_3. This behavior is a characteristic of the FW-BIC [27]. Moreover, the lower resonance reappears by slightly shifting from the FW-BIC position. To provide deeper insight into the behavior of FW-BIC, we present in Figs. 7(c)–7(g) the theoretical DOS (blue solid lines) and the derivative of the Friedel phase $\frac{d\theta_F}{d\omega}$ (green dashed lines) spectra for some values of d_3. The experimental results of $\frac{d\theta_F}{d\omega}$ are plotted in red open circles. Good agreement is obtained between all these quantities, meaning the possibility of measuring the DOS using the determinant of the scattering matrix [Eq. (13)] even in the presence of
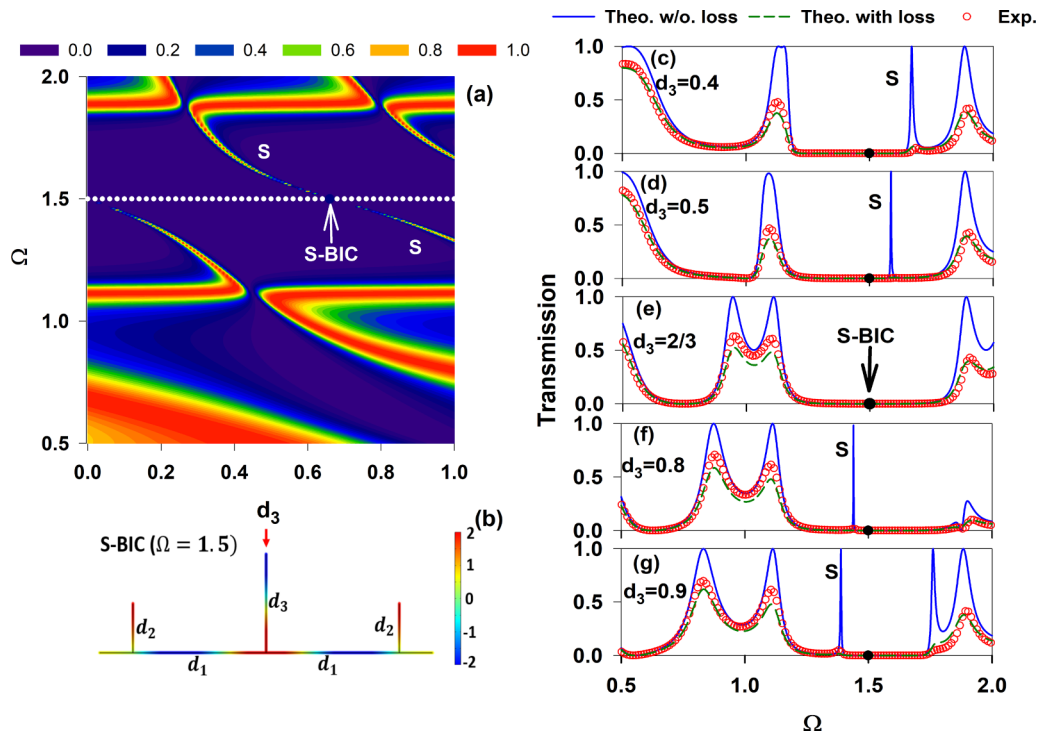
FIG. 6. (a) Theoretical variation of the transmission magnitude vs Ω and d_3 in the lossless symmetric cavity [Fig. 1(a)] with $d_2 = \frac{1}{3}$. (b) Snapshot of the electric field amplitude of the symmetric bound state in the continuum (S-BIC) for $\Omega = \frac{3}{2}$ and $d_3 = \frac{2}{3}$. (c)–(g) Transmission spectra for some values of d_3. Blue and green curves represent theoretical results in the absence and presence of loss, respectively, while the red open circles correspond to the experimental data. The full circles indicate the position of the transmission zero, while the vertical arrow in (e) indicates the S-BIC position.

loss. When d_3 increases, the two interacting resonances in Figs. 7(c)–7(g) approach each other when d_3 tends to 0.5, and the width of the lower resonance (solid arrow) shrinks and reduces to zero at $d_3 = 0.5$ [Fig. 7(e)], giving rise to a FW-BIC, whereas the upper resonance (dashed arrow) still exists as a broad Breit-Wigner resonance in the vicinity of the FW-BIC. By increasing d_3 [Figs. 7(f) and 7(g)], the FW-BIC transforms to a resonance with a finite width below $\Omega = 1$. Furthermore, the upper resonance remains broad, and its position gets closer to $\Omega = 1$. To better explain the evolution of the linewidth of the two resonances in Figs. 7(c)–7(g), we present in the inset of Fig. 7(g) the full width at half maximum (FWHM) for the lower (red curve) and upper (blue curve) resonances as a function of d_3. The linewidth of the lower resonance (γ_-) decreases as far as d_3 tends to 0.5 and vanishes at $d_3 = 0.5$, giving rise to a FW-BIC, whereas the FWHM of the upper resonance (γ_+) increases with d_3 and becomes wider at $d_3 = 0.5$ and then decreases for $d_3 > 0.5$. The behavior of the widths γ_- and γ_+ of the two interacting modes is a characteristic of the FW-BIC [27].

This behavior is also observed in the transmission intensity graph [Fig. 7(b)]. The white and pink dotted curves show the positions of the transmission zeros induced by stubs d_2 and d_3 (i.e., $C_2 = 0$ and $C_3 = 0$), respectively. However, the behavior of the two interacting resonances is slightly different from that of the DOS. One can see here also a shrinking of the lower resonance when d_3 tends to 0.5 and its transformation to a BIC at $\Omega = 1$ and $d_3 = 0.5$, whereas the upper branch becomes more lossy and is significantly impacted by stub

d_3. The transmission zero induced by stub d_3 (pink branch) crosses the upper resonance and leads to the cutoff of this resonance around $\Omega = 1.15$ and $d_3 = 0.45$. For $d_3 < 0.5$, the two resonances fall between two transmission zeros, giving rise to two Fano resonances. However, for $d_3 > 0.5$, only the lower resonance falls between two transmission zeros, giving rise to EIT resonance. At the crossing point around $d_3 = 0.5$, the intensity of the upper resonance becomes very weak due to its coincidence with transmission zero. All these behaviors are illustrated in the transmission spectra displayed in Figs. 7(h)–7(l). The experiment (red curves) reproduces very well the theoretical (green curves) results. The full circles on the frequency axis indicate the position of the transmission zeros induced by stub d_2 [white branch in Fig. 7(b)] and d_3 [pink branch in Fig. 7(b)]. For $d_3 = 0.3$ [Fig. 7(h)], one can observe the existence of two Fano-shaped resonances (indicated by solid and dashed arrows) squeezed between two transmission zeros and corresponding to the upper and lower resonances, respectively, in Fig. 7(b). For $d_3 = 0.4$ [Fig. 7(i)], the two resonances shrink more between the two transmission zeros; the lower resonance keeps the Fano shape, while the upper resonance undergoes an alteration of its shape. For $d_3 = 0.5$ [Fig. 7(j)], the two transmission zeros fall at the same frequency $\Omega = 1$, the lower resonance becomes hidden, leading to the FW-BIC, while the upper one remains very weak due to its proximity to the transmission zeros. When we shift from the BIC position [Figs. 7(k) and 7(l)], the lower resonance reappears as a symmetric EIT resonance inserted between two transmission zeros, while the upper resonance behaves
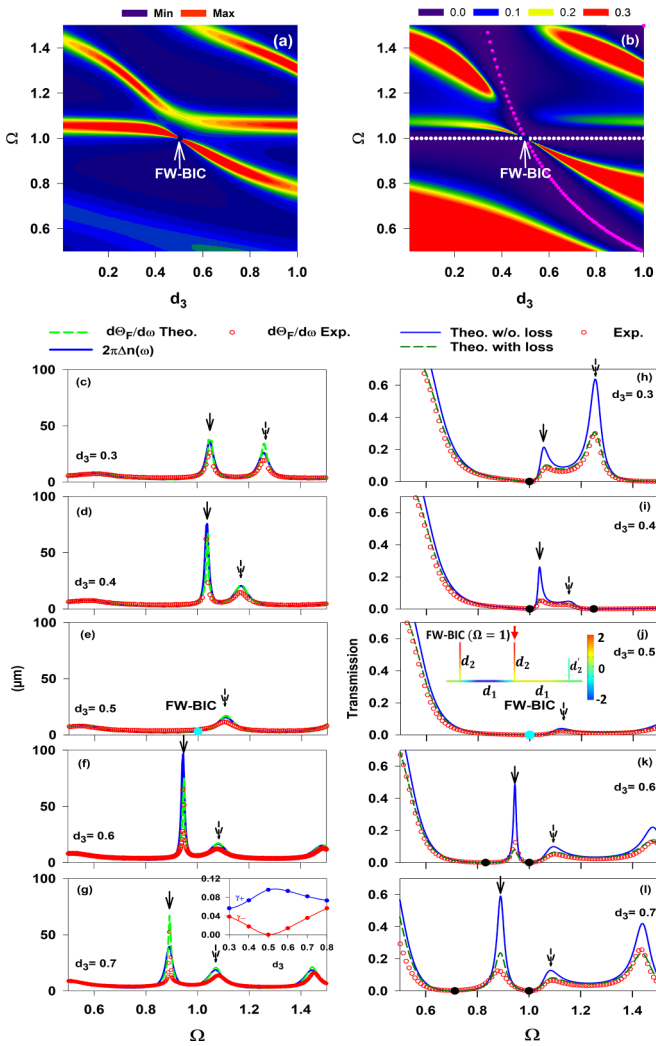
FIG. 7. (a) Theoretical variation of the density of states (DOS) and (b) transmission magnitude vs Ω and d_3 in the lossless asymmetric cavity. The white arrows indicate the Friedrich-Wintgen bound state in the continuum (FW-BIC) position. (c)–(g) (left panel) DOS (blue lines) and the derivative of the Friedel phase $\frac{d\theta_F}{d\omega}$ spectra for different values of d_3. The theoretical results of $\frac{d\theta_F}{d\omega}$ (green dashed lines) are validated by the experimental measurements (red open circles). The solid and dashed arrows correspond to the positions of the lower and higher resonances, respectively. The linewidths of the upper (blue curve) and lower (red curve) DOS resonances are shown in the inset of (g). (h)–(l) (right panel) Transmission spectra for some values of d_3. The inset of (j) gives the electric field map of the FW-BIC. The solid and dashed curves represent theoretical results without and with loss, respectively, while open circles represent experimental data.

like Fano resonance. We have also calculated the electric field distribution associated with the FW-BIC in the inset of Fig. 7(j) to show its expansion in the triple-stub cavity. The BIC is confined in the left U-shaped cavity made of (d_2-d_1-d_2) without propagation throughout the rest of the system. Indeed, we can demonstrate analytically that the FW-BIC is induced by the left U cavity, and it is independent of the surrounding environment including the stub of length d_2' on the right side. However, the length of stub d_2' plays an important role in the

coupling of the BIC induced by the left U cavity (d_2-d_1-d_2) with the resonance induced by the right U cavity (d_2-d_1-d_2'). A detailed analysis of the mechanism behind FW-BICs and FP-BICs and their applications to the triple-stub cavity is shown in Supplemental Material SM6 [60].

III. TRIPLE-STUB CAVITY WITH ONE OR TWO PORTS FROM ONE SIDE

The number of BICs in the triple-stub cavity depends on how it is connected to semi-infinite waveguides. In this section, we will show that, if the triple-stub cavity is attached vertically to two semi-infinite wires from one side [Fig. 1(b)] or to only one semi-infinite wire [Fig. 1(c)], other BICs can occur in addition to the previous BICs discussed in Sec. II.

A. Triple-stub cavity with two ports from one side

Consider first the cavity in contact with two semi-infinite waveguides [Fig. 1(b)] from one side. Indeed, the advantage of such a vertical structure lies in the possibility of deducing the eigenmodes of the isolated cavity, i.e., the system before being attached to the waveguide, with either the Neumann boundary condition (NBC; vanishing of the magnetic field $H = 0$) or the Dirichlet boundary condition (DBC; vanishing of the electric field $E = 0$) at its bottom termination. Indeed, it was shown that such eigenmodes can be obtained from the maxima and minima of transmission through the vertical cavity, respectively [62,63].

The expression of the transmission t_v and reflection r_v coefficients across the cavity in Fig. 1(c) are given as follows (see Supplemental Material SM1 [60]):

$$t_v = \frac{2\tau}{2\tau - j\rho}, \tag{14a}$$

and

$$r_v = \frac{-j\rho}{2\tau - j\rho}, \tag{14b}$$

where τ and ρ are given by

$$\tau = C_2[C_0(2C_1C_3 - S_1S_3) - C_2C_3], \tag{15a}$$

and

$$\rho = C_0(C_0S_3 + 2S_0C_3), \tag{15b}$$

with $C_0 = \cos[k(d_1 + d_2)]$ and $S_0 = \sin[k(d_1 + d_2)]$.

The eigenmodes of the whole system [Fig. 1(b)] can be obtained from the denominator of the the expressions of t_v and r_v or, equivalently, from the poles of its Green's function, namely,

$$2\tau - j\rho = 0. \tag{16}$$

Equation (16) holds if

$$\tau = 0 \quad \text{and} \quad \rho = 0, \tag{17}$$

which gives the eigenmodes of DBC and NBC cavities, respectively.

In addition to the S-BIC and AS-BIC found in the previous section [Eqs. (4), (6a), and (6b)], Eqs. (15a), (15b), and (16) lead to other BICs when both the real and imaginary parts

vanish simultaneously, that is,

$$C_0 = 0 \quad \text{and} \quad C_3 = 0. \tag{18}$$

From Eq. (18) [i.e., $k(d_1 + d_2) = (2m_0 + 1)\frac{\pi}{2}$ and $kd_3 = (2m_3 + 1)\frac{\pi}{2}$], one can deduce the commensurability between $d_1 + d_2$ and d_3 as well as the corresponding BIC frequency, namely,

$$\frac{d_3}{d_1 + d_2} = \frac{2m_3 + 1}{2m_0 + 1}, \tag{19a}$$

and

$$\Omega = \frac{kd_1}{\pi} = \frac{2m_0 + 1}{2\left(1 + \frac{d_2}{d_1}\right)}. \tag{19b}$$

Notice that we can easily demonstrate that, when Eq. (4) giving D-BIC holds, the transmission [Eq. (14a)] vanishes, while if Eq. (18) giving the additional BICs is satisfied, then the transmission [Eq. (14a)] becomes unity.

In what follows, we will give some numerical calculations and experimental validation of the above analytical results. Also, we chose $\frac{d_2}{d_1} = \frac{1}{2}$ and d_3 variable, as in Sec. II. Figure 8(a) gives the dispersion curves as a function of d_3 for the triple-stub cavity with the NBC (cyan curves) and DBC (pink curves). These curves are given by $\rho = 0$ and $\tau = 0$ [Eq. (17)], respectively. The cyan and pink circles give the experimental data obtained, respectively, from the maxima and minima of the transmission coefficient (see below). As mentioned previously, the crossing of $\tau = 0$ and $\rho = 0$ gives rise to BICs. Around $\Omega = 1$, we obtain similar results as presented above, namely, the AS-BIC at $\Omega = 1$ (whatever the value of d_3) as well as the D-BIC at $d_3 = 0.5$. However, above $\Omega = 1.5$, there exist two additional BICs when the cavity is in contact with two wires [Fig. 1(b)] from only one side. These two BICs, labeled BIC$_I$ and BIC$_{II}$, are given by the pairs ($m_3 = 0$ and $m_0 = 2$) and ($m_3 = 1$ and $m_0 = 2$) in Eqs. (19a) and (19b) with $\frac{d_3}{d_1} = \frac{3}{10}$, $\frac{d_3}{d_1} = \frac{9}{10}$, and $\Omega = \frac{5}{3}$, respectively. The D-BIC for $d_3 = 0.5$ and $\Omega = 1$ arises as the intersection of two curves associated with $\tau = 0$ and one curve associated with $\rho = 0$; hence, the D-BIC coincides with transmission zero (see below). However, BIC$_I$ and BIC$_{II}$ correspond to the intersection of two curves associated with $\rho = 0$ and one curve associated with $\tau = 0$. Consequently, these two BICs coincide with a zero of reflection (i.e., the maximum of transmission). Figures 8(b) and 8(c) give the transmission intensity (in color scale) of the vertical cavity [Fig. 1(b)] as a function of Ω and d_3. We have provided both the theoretical [Fig. 8(b)] and experimental [Fig. 8(c)] results, and good agreement can be noticed. Here, too, we can see that the BICs appear as zero-width resonances and antiresonances in the transmission spectra (marked by white circles). As mentioned before, the D-BIC coincides with transmission zero, while BIC$_I$ and BIC$_{II}$ coincide with the maximum of transmission. Figures 8(d)–8(i) give some examples of transmission spectra as a function of Ω for certain values of d_3. Solid blue lines represent the theoretical transmission in a lossless system, while the green dashed lines (red open circles) are associated with the theoretical (experimental) results when loss is considered. The experimental measurements are perfectly reproduced by the theoretical calculation (dashed lines). Further, the resonant

mode just above $\Omega = 1$ for $d_3 = 0.2$ [Fig. 8(d)] appears as an asymmetric EIT resonance; then it decreases in frequency when d_3 increases and disappear at $d_3 = \frac{1}{2}$, leading to the S-BIC and thereby to the D-BIC [Fig. 8(g)] when it coincides with the AS-BIC, whereas BIC$_I$ and BIC$_{II}$ are associated with the maximum transmission for $d_3 = 0.3$ and 0.9, which are indicated by full black circles at $\Omega = \frac{5}{3}$, as depicted in Figs. 8(e) and 8(i). By slightly deviating from the BIC position, these latter transform into antiresonances squeezed between two maxima of transmission (reflection zero), giving rise to the so-called EIR resonance, as shown in Figs. 8(d), 8(f), and 8(h). An analysis of the electric field map associated with BIC$_I$ [Fig. 8(j)] clearly shows that this mode is confined in the upper U-shaped cavity (d_2-d_1-d_3) without any radiation in the rest of the system, even though it corresponds to the maximum of transmission. It is worth mentioning that the electric field of the AS-BIC and D-BIC gives the same behavior as shown previously in Fig. 4.

B. Triple-stub cavity with one port from one side

Another interesting configuration consists of putting the cavity in contact with only one wire from the left side [Fig. 1(c)]. The different modes in the cavity can be investigated by means of the reflection coefficient given by (see Supplemental Material SM1 [60])

$$r = \frac{\tau + j\rho}{\tau - j\rho}, \tag{20}$$

where τ and ρ are given by Eqs. (15a) and (15b).

It is worth noting that, in a perfect lossless system, the reflection amplitude reaches unity ($R = |r|^2 = 1$), while in a real system, owing to the absorption, $R = 1 - A$, where A is the absorption intensity.

The reflection intensity provides different resonant modes of the cavity, including BICs. Indeed, due to the loss, the reflection rate does not reach unity, and the resonant modes of the system appear as dips in the reflection spectra. For a lossy system, Fig. 9 reveals the behavior of different BICs and resonances of the cavity, both theoretically [Fig. 9(a)] and experimentally [Fig. 9(b)], in the reflection spectra as a function of Ω and d_3. Here also, the theory matches well with the experiment. Indeed, the D-BIC, BIC$_I$, and BIC$_{II}$ already discussed in Fig. 8, appear here also. As earlier demonstrated (Sec. II A), the disappearance of the resonance at $d_3 = \frac{1}{2}$ and $\Omega = 1$ [Eq. (7)] indicates the presence of a D-BIC. Likewise, when the length d_3 is appropriately chosen [Eq. (19a)], we observe a hidden resonance around $\Omega = \frac{5}{3}$ for $d_3 = 0.3$ and 0.9; this behavior indicates the presence of BIC$_I$ and BIC$_{II}$. Figures 9(c)–9(h) depict the behavior of reflection (black curves) and absorption (red curves) through the lossy system as a function of Ω for various values of d_3. The theoretical (continuous curves) and experimental (open red circles) results are in good agreement. For $d_3 = 0.2$ [Fig. 9(c)], the reflection resonance tends to zero around $\Omega = 1.23$, whereas the absorption reaches a maximum value of $A = 0.99$. Furthermore, as d_3 increases, the resonance width decreases in the reflection spectra, and its intensity increases [Fig. 9(d)], leading to the formation of a D-BIC at $d_3 = 0.5$ [Fig. 9(f)]. This mode appears as a hidden resonance with a zero width,
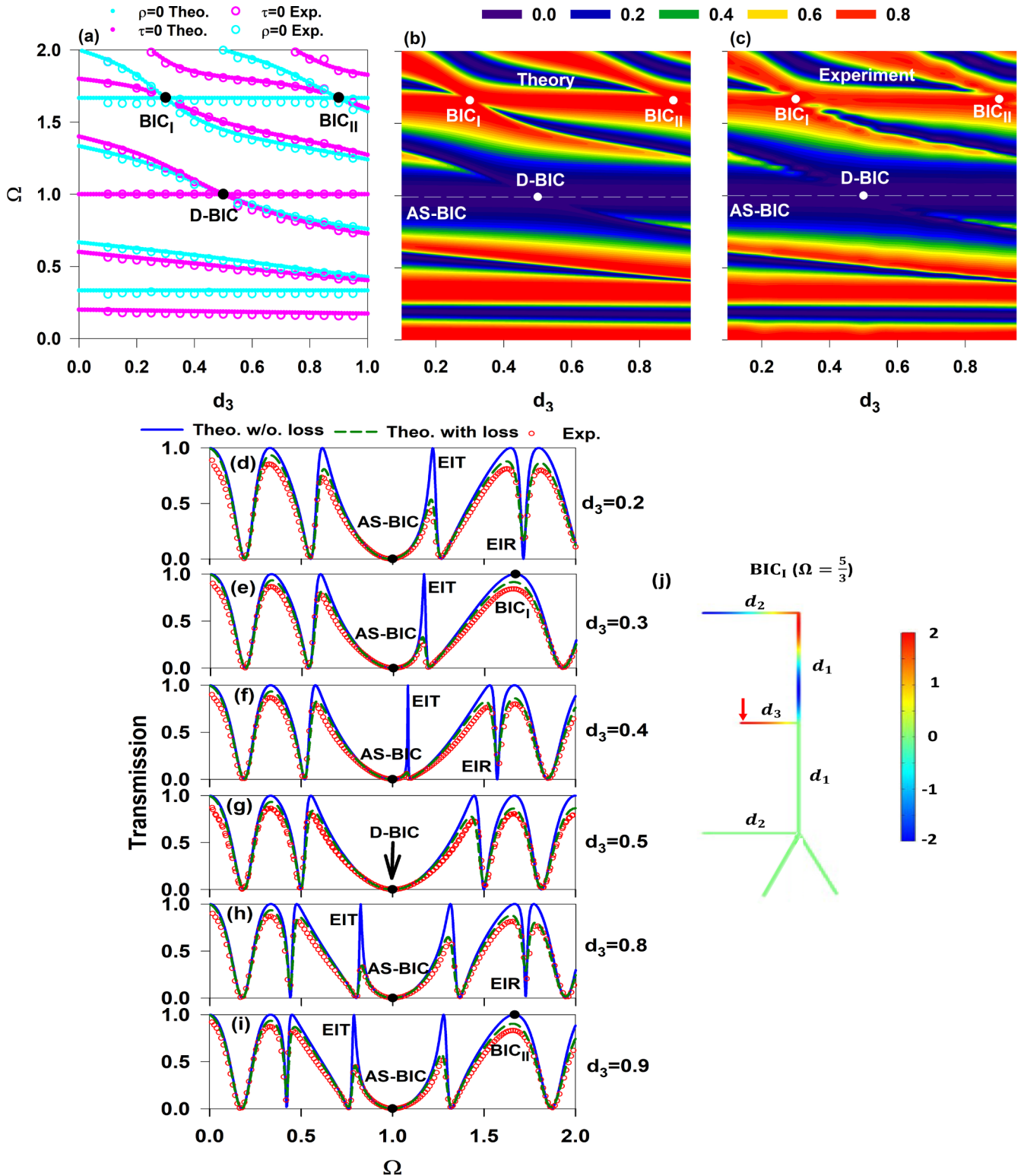
FIG. 8. (a) Dispersion curves of the vertical cavity in Fig. 1(c) with Neumann boundary condition (NBC; $\rho = 0$, cyan curves) and Dirichlet boundary condition (DBC; $\tau = 0$, pink curves) as a function of d_3 and Ω. The cyan and pink circles give the experimental data obtained, respectively, from the maxima and minima of the transmission coefficient. (b) Theoretical and (c) experimental variation of the transmission magnitude through the lossy cavity. The horizontal dashed lines show the position of the antisymmetric bound state in the continuum (AS-BIC). (d)–(i) Transmission spectra as a function of Ω for various values of d_3. The dashed green lines (open red circles) represent the theoretical (experimental) results in the presence of losses, while solid blue lines represent the theoretical results for a lossless system. The full circles determine the BIC position, while the vertical arrow in (g) shows the doubly degenerate BIC (D-BIC). (j) Snapshot of the electric field amplitude of BIC$_I$ at $\Omega = \frac{5}{3}$ and $d_3 = 0.3$ in (e).
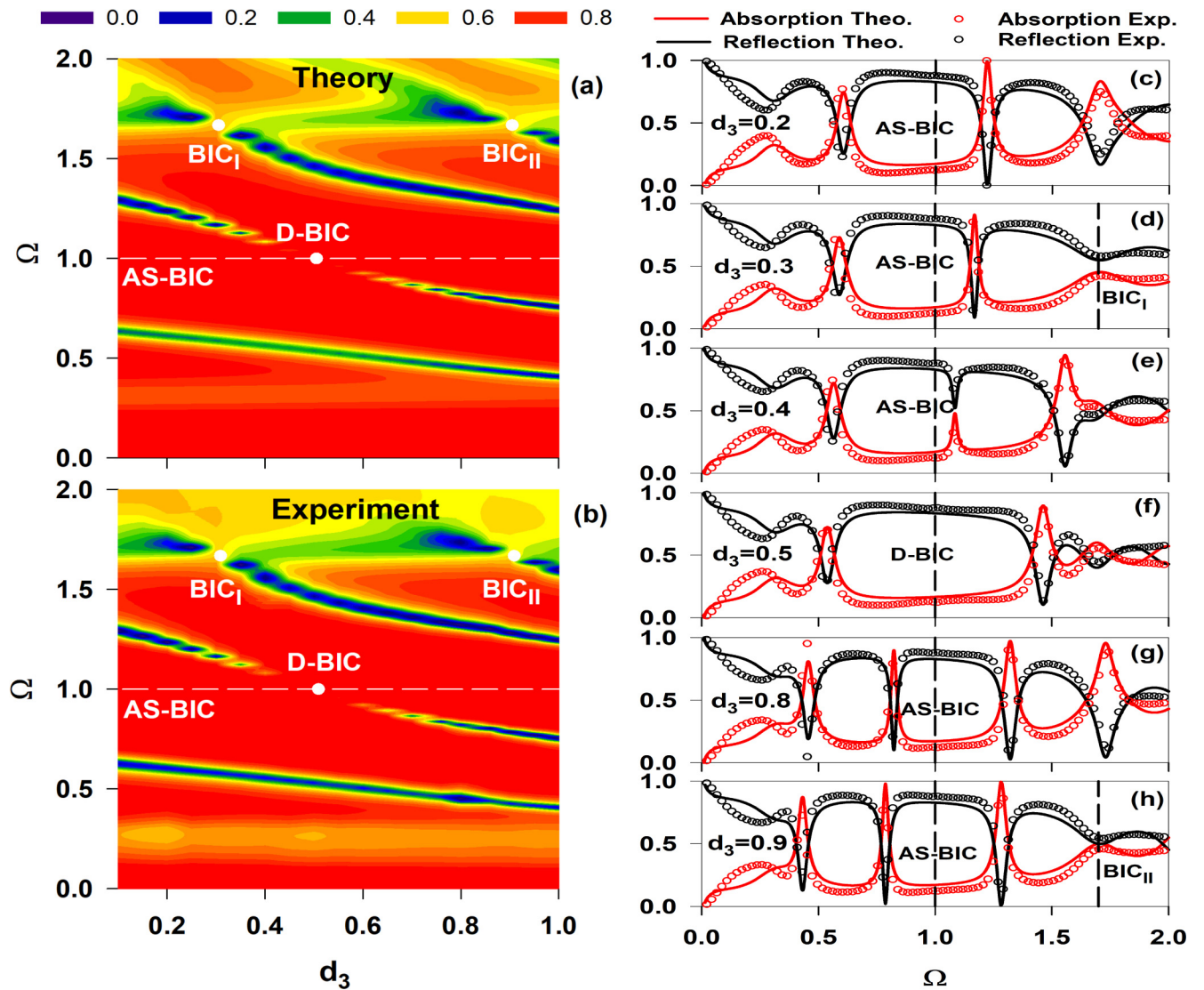
FIG. 9. (a) Theoretical and (b) experimental variation of the reflection magnitude for the cavity in Fig. 1(b) as a function of Ω and d_3. (c)–(h) Variation of reflection (black curves) and absorption (red curves) spectra vs Ω for different values of length d_3. Black dashed lines indicate the BIC positions.

giving rise to a plateau in the reflection ($R \simeq 0.9$), while the absorption approaches zero ($A \simeq 0.1$). Similarly, around BIC_I and BIC_{II} [Figs. 9(d) and 9(h)], one can see the transformation of the resonances into hidden resonances at $\Omega = \frac{5}{3}$ for $d_3 = 0.3$ and 0.9 (indicated by dashed lines), then their reappearance by slightly detuning stub d_3 from the BIC position. Moreover, let us point out the possibility to reach a near-perfect absorption [14] for some frequencies, as shown in Figs. 9(c), 9(g), and 9(h), where the wave penetrates the cavity without back reflection. In addition to the reflection intensity, the reflection delay time τ_R and DOS can also be useful for analyzing the existence and behavior of the BICs in the triple-stub cavity (see Supplemental Material SM7 [60]).

IV. CONCLUSIONS

In this paper, we have investigated, both theoretically and experimentally, the existence and behavior of resonant modes

and BICs in a triple-stub cavity made of a stub of length d_3 inserted between two stubs of length d_2; all stubs are separated by a segment of length d_1. The cavity can be either placed between two semi-infinite waveguides from both sides or just one or two waveguides from one side. In the case of a symmetric cavity inserted between two waveguides, we have demonstrated the condition of commensurability that should be satisfied by d_1, d_2, and d_3 as well as the corresponding frequencies to get a S-BIC and an AS-BIC of FP type. We have shown that these two BICs can cross each other, giving rise to a D-BIC. This property cannot be fulfilled in the case of a cavity with just two stubs. By slightly detuning the length of one of the two stubs of length d_2 by a small amount δ, the symmetry of this cavity is broken, and one assists in lifting of the degeneracy of the two BICs; one of the two BICs remains constant, whereas the second BIC becomes a resonance with a given width that can be tuned by varying δ. This behavior is analogous to the so-called FW-BIC obtained

from the interaction of two modes in the same cavity. Also, we have investigated the effect of the presence of one or two waveguides, placed on one side of the cavity, on the number of BICs. We have shown that, in addition to the BICs obtained in the symmetric cavity, which are independent of the number of ports surrounding the cavity, there exist other BICs induced by the stubs when one port is removed. These additional BICs are evidenced by analyzing the reflection spectra for the cavity in contact with one port from one side or through an analysis of the transmission spectra of the cavity placed vertically along two ports from one side. The latter configuration enables the extraction of all the eigenmodes of the cavity, including the different BICs. When deviating from the BIC condition, the latter transforms into either EIT, EIR, or Fano resonance. Furthermore, near-perfect absorption can be accomplished with the triple-stub cavity at some frequencies.

All the analytical results are obtained from an analysis of the DOS, scattering matrix, and transmission and reflection coefficients using the Green's function method, whereas the experimental measurements are performed on coaxial cables operating in the radiofrequency domain. All these results can be transposed easily to plasmonic nanocircuits based on MIM waveguides operating in the infrared domain [63,64]. Such structures can support BICs and induced resonances and can be used as high-performing device sensors. We have given an example illustrating a BIC and EIT resonance in silver-air-silver nanoplasmonic waveguides operating in the infrared domain (see Supplemental Material SM8 [60]). Also, these results can be applied to acoustic waveguides [37] as well as solid-liquid phononic multilayered systems where the solid layer acts as a resonator inside the liquid [65]. All these works are in progress.

[1] L. Dobrzynski, A. Akjouj, E. H. El Boudouti, G. Lévêque, H. Al-Wahsh, Y. Pennec, C. Ghouila-Houri, A. Talbi, B. Djafari-Rouhani, and Y. Jin, *Photonics* (Elsevier, Amsterdam, 2021).

[2] A. E. Miroshnichenko, S. Flach, and Y. S. Kivshar, Fano resonances in nanoscale structures, Rev. Mod. Phys. **82**, 2257 (2010).

[3] M. V. Rybin, D. S. Filonov, P. A. Belov, Y. S. Kivshar, and M. F. Limonov, Switching from visibility to invisibility via Fano resonances: Theory and experiment, Sci. Rep. **5**, 8774 (2015).

[4] M. Fleischhauer, A. Imamoglu, and J. P. Marangos, Electromagnetically induced transparency: Optics in coherent media, Rev. Mod. Phys. **77**, 633 (2005).

[5] N. Scharnhorst, J. Cerrillo, J. Kramer, I. D. Leroux, J. B. Wubbena, A. Retzker, and P. O. Schmidt, Experimental and theoretical investigation of a multimode cooling scheme using multiple electromagnetically-induced-transparency resonances, Phys. Rev. A **98**, 023424 (2018).

[6] S. F. Mingaleev, A. E. Miroshnichenko, and Y. S. Kivshar, Coupled-resonator-induced reflection in photonic-crystal waveguide structures, Opt. Express **16**, 11647 (2008).

[7] U. Fano, Effects of configuration interaction on intensities and phase shifts, Phys. Rev. **124**, 1866 (1961).

[8] S. E. Harris, Electromagnetically induced transparency, Phys. Today **50**(7), 36 (1997).

[9] J. von Neumann and E. P. Wigner, Über merkwürdige diskrete Eigenwerte, Phys. Z. **30**, 465 (1929).

[10] C. W. Hsu, B. Zhen, A. D. Stone, J. D. Joannopoulos, and M. Soljacic, Bound states in the continuum, Nat. Rev. Mater. **1**, 16048 (2016).

[11] S. I. Azzam and A. V. Kildishev, Photonic bound states in the continuum: From basics to applications, Adv. Opt. Mater. **9**, 2001469 (2021).

[12] S. Sun, Y. Ding, H. Li, P. Hu, C.-W. Cheng, Y. Sang, F. Cao, Y. Hu, A. Alu, D. Liu *et al.*, Tunable plasmonic bound states in the continuum in the visible range, Phys. Rev. B **103**, 045416 (2021).

[13] A. Mouadili, E. H. El Boudouti, A. Soltani, A. Talbi, A. Akjouj, and B. Djafari-Rouhani, Theoretical and experimental evidence of Fano-like resonances in simple monomode photonic circuits, J. Appl. Phys. **113**, 164101 (2013).

[14] A. Mouadili, E. H. El Boudouti, A. Soltani, A. Talbi, B. Djafari-Rouhani, A. Akjouj, and K. Haddadi, Electromagnetically induced absorption in detuned stub waveguides: A simple analytical and experimental model, J. Phys.: Condens. Matter **26**, 505901 (2014).

[15] P. S. Pankin, B. R. Wu, J. H. Yang, K. P. Chen, I. V. Timofeev, and A. F. Sadreev, One-dimensional photonic bound states in the continuum, Commun. Phys. **3**, 91 (2020).

[16] H. Takahashi, E. Kassa, C. Christoforou, and M. Keller, Strong coupling of a single ion to an optical cavity, Phys. Rev. Lett. **124**, 013602 (2020).

[17] A. A. Bogdanov, K. L. Koshelev, P. V. Kapitanova, M. V. Rybin, S. A. Gladyshev, Z. F. Sadriev, K. B. Samusev, Y. S. Kivshar, and M. F. Limonov, Bound states in the continuum and Fano resonances in the strong mode coupling regime, Adv. Photon. **1**, 016001 (2019).

[18] S. Khattou, Y. Rezzouk, M. Amrani, M. El Ghafiani, A. Talbi, and B. Djafari-Rouhani, Friedrich-Wintgen bound states in the continuum in a photonic and plasmonic T-shaped cavity: Application to filtering and sensing, Phys. Rev. Appl. **20**, 044015 (2023).

[19] K. Koshelev, G. Favraud, A. Bogdanov, Y. Kivshar, and A. Fratalocchi, Nonradiating photonics with resonant dielectric nanostructures, Nanophotonics **8**, 725 (2019).

[20] Z. Qi, G. Hu, B. Liu, Y. Li, C. Deng, P. Zheng, F. Wang, L. Zhao, and Y. Cui, Plasmonic nanocavity for obtaining bound state in the continuum in silicon waveguides, Opt. Express **29**, 9312 (2021).

[21] Y. Rezzouk, S. Khattou, M. Amrani, A. Noual, E. H. El Boudouti, A. Talbi, and B. Djafari-Rouhani, Bound states in the continuum and induced resonances in a simple plasmonic waveguide with sensing application, Photonics **10**, 1284 (2023).

[22] K. Koshelev, S. Lepeshov, M. Liu, A. Bogdanov, and Y. Kivshar, Asymmetric metasurfaces with high-Q resonances governed by bound states in the continuum, Phys. Rev. Lett. **121**, 193903 (2018).

[23] S. Han, P. Pitchappa, W. Wang, Y. K. Srivastava, M. V. Rybin, and R. Singh, Extended bound states in the continuum with

symmetry-broken terahertz dielectric metasurfaces, Adv. Opt. Mater. **9**, 2002001 (2021).

[24] Y. X. Zhang, Q. Lin, X. Q. Yan, L. L. Wang, and G. D. Liu, Flat-band Friedrich-Wintgen bound states in the continuum based on borophene metamaterials, Opt. Express **32**, 10669 (2024).

[25] X. Gao, B. Zhen, M. Soljacic, H. Chen, and C. W. Hsu, Bound states in the continuum in fiber Bragg gratings, ACS Photonics **6**, 2996 (2019).

[26] Z. F. Sadrieva, M. A. Belyakov, M. A. Balezin, P. V. Kapitanova, E. A. Nenasheva, A. F. Sadreev, and A. A. Bogdanov, Experimental observation of a symmetry-protected bound state in the continuum in a chain of dielectric disks, Phys. Rev. A **99**, 053804 (2019).

[27] H. Friedrich and D. Wintgen, Physical realization of bound states in the continuum, Phys. Rev. A **31**, 3964 (1985).

[28] D. C. Marinica, A. G. Borisov, and S. V. Shabanov, Bound states in the continuum in photonics, Phys. Rev. Lett. **100**, 183902 (2008).

[29] S. Li, C. Zhou, T. Liu, and S. Xiao, Symmetry-protected bound states in the continuum supported by all-dielectric metasurfaces, Phys. Rev. A **100**, 063803 (2019).

[30] M. V. Rybin, K. L. Koshelev, Z. F. Sadrieva, K. B. Samusev, A. A. Bogdanov, M. F. Limonov, and Y. S. Kivshar, High-*Q* supercavity modes in subwavelength dielectric resonators, Phys. Rev. Lett. **119**, 243901 (2017).

[31] M. Luo and F. Wu, Wavy optical grating: Wideband reflector and Fabry-Perot bound states in the continuum, Phys. Rev. A **106**, 063514 (2022).

[32] X. Li, E. Maqbool, and Z. Han, Narrowband mid-infrared thermal emitters based on the Fabry-Perot type of bound states in the continuum, Opt. Express **31**, 20338 (2023).

[33] A. F. Sadreev, Interference traps waves in open system: Bound states in the continuum, Rep. Prog. Phys. **84**, 055901 (2021).

[34] Z. Liu, X. Li, C. Chen, X. Wang, W. Gao, W. Ye, L. Li, and J. Liu, Bound states in the continuum in asymmetric one-dimensional photonic crystal systems guided by anisotropy, Opt. Express **31**, 8384 (2023).

[35] H. M. Doeleman, F. Monticone, W. den Hollander, A. Alù, and A. F. Koenderink, Experimental observation of a polarization vortex at an optical bound state in the continuum, Nat. Photon. **12**, 397 (2018).

[36] S. Mesli, H. Yala, M. Hamidi, A. BelKhir, and F. I. Baida, High performance for refractive index sensors via symmetry-protected guided mode resonance, Opt. Express **29**, 21199 (2021).

[37] L. Huang, B. Jia, A. S. Pilipchuk, Y. Chiang, S. Huang, J. Li, C. Shen, E. N. Bulgakov, F. Deng, D. A. Powell *et al.*, General framework of bound states in the continuum in an open acoustic resonator, Phys. Rev. Appl. **18**, 054021 (2022).

[38] M. S. Sidorenko, O. N. Sergaeva, Z. F. Sadrieva, C. Roques-Carmes, P. S. Muraev, D. N. Maksimov, and A. A. Bogdanov, Observation of an accidental bound state in the continuum in a chain of dielectric disks, Phys. Rev. Appl. **15**, 034041 (2021).

[39] Y. Jin, E. H. El Boudouti, Y. Pennec, and B. Djafari-Rouhani, Tunable Fano resonances of Lamb modes in a pillared metasurface, J. Phys. D: Appl. Phys. **50**, 425304 (2017).

[40] W. Wang, Y. K. Srivastava, T. C. Tan, Z. Wang, and R. Singh, Brillouin zone folding driven bound states in the continuum, Nat. Commun. **14**, 2811 (2023).

[41] F. Wu, X. Qi, M. Qin, M. Luo, Y. Long, J. Wu, Y. Sun, H. Jiang, T. Liu, S. Xiao *et al.*, Momentum mismatch driven bound states in the continuum and ellipsometric phase singularities, Phys. Rev. B **109**, 085436 (2024).

[42] Y. Plotnik, O. Peleg, F. Dreisow, M. Heinrich, S. Nolte, A. Szameit, and M. Segev, Experimental observation of optical bound states in the continuum, Phys. Rev. Lett. **107**, 183901 (2011).

[43] J. Jin, X. Yin, L. Ni, M. Soljacic, B. Zhen, and C. Peng, Topologically enabled ultrahigh-*Q* guided resonances robust to out-of-plane scattering, Nature (London) **574**, 501 (2019).

[44] Y. Rezzouk, M. El Ghafiani, S. Khattou, M. Amrani, E. H. El Boudouti, A. Talbi, and B. Djafari-Rouhani, High-*Q* resonant modes in periodic stubbed structure, Lect. Notes Electr. Eng. **954**, 223 (2023).

[45] C. Shi, J. Hu, X. Liu, J. Liang, J. Zhao, H. Han, and Q. Zhu, Double-layer symmetric gratings with bound states in the continuum for dual-band high-*Q* optical sensing, Beilstein J. Nanotechnol. **13**, 1408 (2022).

[46] Z. Li, Y. Xiang, S. Xu, and X. Dai, Ultrasensitive terahertz sensing in all-dielectric asymmetric metasurfaces based on quasi-BIC, J. Opt. Soc. Am. B **39**, 286 (2022).

[47] Z. Yu, X. Xi, J. Ma, H. K. Tsang, C.-L. Zou, and X. Sun, Photonic integrated circuits with bound states in the continuum, Optica **6**, 1342 (2019).

[48] F. Yesilkoy, E. R. Arvelo, Y. Jahani, M. Liu, A. Tittl, V. Cevher, Y. Kivshar, and H. Altug, Ultrasensitive hyperspectral imaging and biodetection enabled by dielectric metasurfaces, Nat. Photon. **13**, 390 (2019).

[49] R. E. Jacobsen, A. Krasnok, S. Arslanagic, A. V. Lavrinenko, and A. Alú, Boundary-induced embedded eigenstate in a single resonator for advanced sensing, ACS Photon. **9**, 1936 (2022).

[50] D. N. Maksimov, V. S. Gerasimov, A. A. Bogdanov, and S. P. Polyutov, Enhanced sensitivity of an all-dielectric refractive index sensor with an optical bound state in the continuum, Phys. Rev. A **105**, 033518 (2022).

[51] A. Kodigala, T. Lepetit, Q. Gu, B. Bahari, Y. Fainman, and B. Kanté, Lasing action from photonic bound states in continuum, Nature (London) **541**, 196 (2017).

[52] S. T. Ha, Y. H. Fu, N. K. Emani, Z. Pan, R. M. Bakker, R. Paniagua-Dominguez, and A. I. Kuznetsov, Directional lasing in resonant semiconductor nanoantenna arrays, Nat. Nanotechnol **13**, 1042 (2018).

[53] M. S. Hwang, H. C. Lee, K. H. Kim, K. Y. Jeong, S. H. Kwon, K. Koshelev, Y. Kivshar, and H. G. Park, Ultralow-threshold laser using super-bound states in the continuum, Nat. Commun. **12**, 4135 (2021).

[54] J. M. Foley, S. M. Young, and J. D. Phillips, Symmetry-protected mode coupling near normal incidence for narrow-band transmission filtering in a dielectric grating, Phys. Rev. B **89**, 165111 (2014).

[55] K. K. Voo, Trapped electromagnetic modes in forked transmission lines, Wave Motion **45**, 795 (2008).

[56] N. W. Ashcroft and N. D. Mermin, *Solid State Physics* (Saunders College Publishing, Philadelphia, 1976).

[57] J. Friedel, The distribution of electrons around impurities in monovalent metals, Philos. Mag. **43**, 153 (1952).

[58] H-W. Lee, Generic transmission zeros and in-phase resonances in time-reversal symmetric single channel transport, Phys. Rev. Lett. **82**, 2358 (1999).

[59] C. Texier, Scattering theory on graphs: II. The Friedel sum rule, J. Phys. A: Math. Gen. **35**, 3389 (2002).

[60] See Supplemental Material at http://link.aps.org/supplemental/10.1103/PhysRevB.109.235431 for details on the analytical calculation of the transmission and reflection coefficients through a triple-stub cavity grafted between two ports either horizontally or vertically as well as the reflection coefficient of the symmetric cavity attached to only one wire at the input (SM1); a comparison between the variation of the DOS and the first derivative of the argument of the determinant of the scattering matrix (the so-called Friedel phase; SM2); details about the experimental procedure and the setup (SM3); a fit of the EIT and Fano resonances by analytical formula (SM4); a comparison between analytical, simulation, and experimental results (SM5); a discussion of the mechanism behind FW and FP BICs (SM6); numerical and experimental comparison between the variation of DOS and the delay time (SM7); and a validation of the analytical results to the plasmonic MIM waveguides operating in the infrared domain (SM8), which includes Ref. [64].

[61] S. Khattou, M. Amrani, A. Mouadili, E. H. El Boudouti, A. Talbi, A. Akjouj, and Bahram Djafari-Rouhani, Comparison of

density of states and scattering parameters in coaxial photonic crystals: Theory and experiment, Phys. Rev. B **102**, 165310 (2020).

[62] B. Djafari-Rouhani, E. H. El Boudouti, A. Akjouj, L. Dobrzynski, J. O. Vasseur, A. Mir, N. Fettouhi, and J. Zemmouri, Surface states in one-dimensional photonic band gap structures, Vacuum **63**, 177 (2001).

[63] Y. Rezzouk, M. Amrani, S. Khattou, E. H. El Boudouti, and B. Djafari-Rouhani, Plasmonic Tamm states in periodic stubbed MIM waveguides: Analytical and numerical study, J. Opt. Soc. Am. B **39**, 600 (2022).

[64] Z. Qiong-Gan and W. Zhi-Guo, The Green's function method for metal-dielectric-metal SPP waveguide network, Europhys. Lett. **103**, 17004 (2013).

[65] M. Amrani, I. Quotane, C. Ghouila-Houri, E. H. El Boudouti, L. Krutyansky, B. Piwakowski, P. Pernod, A. Talbi, and B. Djafari-Rouhani, Experimental evidence of the existence of bound states in the continuum and Fano resonances in solid-liquid layered media, Phys. Rev. Appl. **15**, 054046 (2021).